JOURNAL OF GUIDANCE, CONTROL, AND DYNAMICS
Vol. 32, No. 5, September–October 2009

Engineless Unmanned Aerial Vehicle Propulsion by Dynamic Soaring

Markus Deittert*
University of the West of England, Bristol, England BS16 1QY, United Kingdom
Arthur Richards†
Bristol University, Bristol, England BS8 1TR, United Kingdom
C. A. Toomer‡
University of the West of England, Bristol, England BS16 1QY, United Kingdom
and
Anthony Pipe§
Bristol Robotics Laboratory, Bristol, England BS16 1QD, United Kingdom

DOI: 10.2514/1.43270

Dynamic soaring is a flight technique which extracts energy from wind gradients with the potential to power small unmanned aerial vehicles in maritime applications. Wind gradients of the required magnitude naturally occur at the air–sea interface due to friction between the waves and the moving air. Suitability of dynamic soaring as a means of propulsion requires clarification of the achievable flight performance and the likelihood of favorable winds. Optimal trajectories for minimal and maximal wind conditions are generated as well as trajectories for optimal cross-country travel. The flight model's differential flatness property is used to simplify the optimization problem. The likelihood of favorable winds is predicted based on long term weather statistics and knowledge of the minimal and maximal permissible wind strengths. Comparison of the likelihood of favorable winds for the wandering albatross and an unmanned aerial vehicle of similar size shows that the ability to fly close to the surface is a key factor governing dynamic soaring performance.

Nomenclature

a_{hi}	=	ith height basis function magnitude, m
a_{xi}	=	ith x-position basis function magnitude, m
a_{yi}	=	ith y-position basis function magnitude, m
b	=	wing span, m
$\mathbf{C}(\mathbf{X})$	=	constraints
C_D	=	drag coefficient
C_{Di}	=	ith drag polynomial coefficient
$\mathbf{C}_{\text{eq}}(\mathbf{X})$	=	equality constraints
C_L	=	lift coefficient
$C_{L,\max}$	=	lift coefficient upper limit
D	=	drag, N
E_{kin}	=	kinetic energy, J
E_{pot}	=	potential energy, J
F	=	force, N
g	=	normal acceleration, m/s^2
h	=	height, m
$h_{\min}$	=	wing tip clearance limit, m
h_R	=	reference height, m
$J(\mathbf{X})$	=	value function
L	=	lift, N
$\mathbf{lb}$	=	vector of lower bounds on $\mathbf{X}$
M	=	number of time points
m	=	UAV mass, kg
N	=	number of frequencies
p	=	surface roughness factor
$\mathbf{r}$	=	position vector
r_h	=	position vector h component, m
r_x	=	position vector x component, m
r_y	=	position vector y component, m
S	=	wing planform area, m^2
T	=	thrust, N
$T_{\max}$	=	upper thrust limit, N
$T_{\min}$	=	lower thrust limit, N
t_f	=	maneuver duration, s
$\mathbf{u}$	=	system input vector
$\mathbf{ub}$	=	vector of upper bounds on $\mathbf{X}$
V	=	airspeed, m/s
V_{CC}	=	cross-country travel rate, m/s
$V_{\max}$	=	upper airspeed limit, m/s
V_R	=	wind speed at reference height, m/s
$V_W(h)$	=	wind speed at height h, m/s
$\mathbf{X}$	=	optimization design vector
$\mathbf{x}$	=	system state vector
$\bar{x}$	=	mean value of x
$\mathbf{y}$	=	system output vector
$\mathbf{z}$	=	vector of differentially flat outputs
γ	=	elevation, rad
ε	=	direction angle of cross-country travel, rad
η_{hi}	=	ith height basis function phase shift
η_{xi}	=	ith x-position basis function phase shift
η_{yi}	=	ith y-position basis function phase shift
μ	=	bank angle, rad
$\mu_{\max}$	=	upper bank angle limit, rad
$\mu_{\min}$	=	lower bank angle limit, rad
ρ	=	air density, kg/m^3
σ	=	standard deviation
Ψ	=	azimuth, rad
$\frac{dV_W}{dh}$	=	wind gradient, 1/s

Received 16 January 2009; revision received 24 April 2009; accepted for publication 27 April 2009.

*Research Student; currently at Bristol Robotics Laboratory, DuPont Building, Coldharbour Lane, Bristol, England BS16 1QD, U.K.

†Lecturer, Department of Aerospace Engineering, Queens Building, University Walk. Member AIAA.

‡Principal Lecturer, Bristol Institute of Technology, Frenchay Campus. Member AIAA.

§Reader in Robotics and Autonomous Systems, DuPont Building, Coldharbour Lane, Bristol, England BS16 1QD, U.K.

I. Introduction

A KEY operational factor of unmanned aerial vehicle (UAV) utility is long endurance flight [1]. Omitting the pilot allows flight times far beyond that of human endurance with a very compact airframe and in the absence of in-flight refueling, fuel capacity is again the limiting factor for endurance. To increase endurance beyond the UAV's fuel capacity, the authors propose to use engineless flight, in particular, exploiting wind gradients. This significantly reduces energy consumption, leaving only the demands of the onboard electronics, and hence increases endurance. The flight technique required for exploiting wind gradients is known as dynamic soaring. Missions such as persistent loitering surveillance, which require long endurance flight over the same area, are suitable applications for UAVs using this technique. Maritime patrol and surveillance is another suitable area of use because of the vast areas which must be searched. The open sea is, furthermore, windy and comparatively free of obstacles.

Dynamic soaring is the key method by which albatrosses achieve flights of several thousands of miles with hardly a flap of their wings [2]. The wandering albatross with its 3-m wing span is of similar size to a small UAV such as Boeing's Scaneagle and due to this similarity the authors take the albatross' flight performance as a baseline model against which dynamic soaring performance of a small UAV is judged.

Wind gradients of sufficient magnitude are commonly found in close proximity to the ground, where they arise due to friction between the moving air mass and the surface. As a result height is limited to approximately 30 m. Conventional soaring requires thermals to be detected before energy can be extracted. This represents a significant problem as thermals are sparsely distributed phenomena of finite size, which can be sensed locally only. In contrast dynamic soaring becomes feasible as soon as the wind strength exceeds a certain threshold level and the problem of locating an exploitable energy source therefore does not arise.

Dynamic soaring was analyzed for the first time by Lord Rayleigh [3] in 1883, based upon his observations of albatrosses in the south Atlantic. More recent publications by Sachs et al. [4], Sachs [5], Zhao [6], and Zhao and Qi [7] are concerned with finding trajectories which minimize the required wind conditions. Using a 3-DOF (degrees of freedom) flight model in Earth fixed coordinates, Sachs et al. [4] give an analytical solution of minimal wind condition trajectories for dynamic soaring. This fundamental solution applies to constant wind gradients only. To investigate realistic nonlinear wind gradients, Sachs uses a numerical multiple shooting approach. Zhao uses a 3-DOF flight model in wind relative coordinates and uses a direct collocation approach in combination with the nonlinear solver NPSOL [8], to find minimal wind condition trajectories for loitering flight [6] and power assisted dynamic soaring [7]. Zhao and Qi's work [7] shows that assistance by an engine allows long duration motion similar to dynamic soaring in cases where the wind speed is less than the minimal required value for engineless flight. However, this facility is beyond the scope of this paper. The work of Sachs and Zhao also shows the importance of a high L/D ratio for dynamic soaring. In this article, the authors first extend the work of Sachs and Zhao by investigating trajectories for *maximal* wind conditions that allow dynamic soaring. Furthermore, we analyze the sensitivity of the minimal and maximal conditions to flight path constraints and physical parameters of the UAV. We then extend our methodology to cross-country flight, investigating directional dependence of minimal and maximal wind conditions and cross-country travel rates. The difference between minimal and maximal wind conditions gives the range of favorable winds. We combine these with weather statistics to predict the likelihood of favorable winds at candidate locations.

Unsuccessful early attempts at manned dynamic soaring in the marine boundary layer by Utgoff and Johnson [9] show that control of the aircraft during dynamic soaring is not a trivial problem. However, Gordon's [10] successful demonstration of energy extraction from wind gradients by a manned glider shows that these control problems are solvable. The authors intend to establish outer bounds on wind conditions and on the likelihood of favorable winds. Thus, only the initial problem of designing trajectories to find maximum and minimum limits on wind conditions is considered in this paper. The problem of an accurate prediction of dynamic soaring performance, which must account for atmospheric turbulence and the effects of the control system, is left for future research.

In the first section we will describe our methodology: the mathematical models for the UAV, wind gradient, and optimization problem for the trajectory. In the later sections we will present our results for maximum and minimum wind conditions, attainable cross-country performance of a typical UAV, and likelihood of favorable weather at candidate locations in the Atlantic Ocean and English Channel.

II. Methodology

A. Wind Model

For the sake of simplicity, it is initially assumed that the UAV flies over a flat surface. Air density is assumed to be constant and homogeneous and the wind blows along the positive x axis at all times. Friction between the surface and moving air mass causes the wind speed to be strongly dependent on the height above the surface. The relation between wind speed V_W and height above the surface h is given by

$$V_W(h) = V_R\left(\frac{h}{h_R}\right)^p \tag{1}$$

Typical values of p [5,11,12] range from 0.1 to 0.143 and the authors follow Sachs's [5] choice of $p = 0.143$. The reference height can be picked arbitrarily and a value of $h_R = 20$ m was chosen. Finding the minimum or maximum reference wind speed at this height, which still permits dynamic soaring, is the task of the numerical optimization process. We assume that V_W changes due to altitude changes only. Hence, its derivative with respect to time can be expressed as

$$\dot{V}_W = \frac{dV_W}{dh}\dot{h} = \frac{pV_R}{h}\left(\frac{h}{h_R}\right)^p \dot{h} \tag{2}$$

A plot of the wind profile and wind gradient profile can be found in Fig. 1. The amount of energy which can be extracted from the wind gradient is related to the gradient's magnitude, which is large at low height values. We will show in Sec. IV that the flight performance depends on how close the vehicle approaches the surface.

B. Flight Model

In this paper we consider two different flyers: a wandering albatross and a similar sized UAV. While they share the same wing span of 3 m, some differences must be considered. First, the UAV's wing profile differs from the albatross. Typical values for lift and drag coefficients for the wandering albatross are given by Sachs [5]. The SD 7037 aerofoil[¶] has been selected for study, because a wing with this aerofoil achieves better performance than the modeled albatross wing in the sense that it produces low drag for larger range of airspeeds and has a superior lift-to-drag ratio. Second, the albatross is a more proactive flyer compared with an autonomous UAV. Pennycuick [13] reports that albatrosses routinely fly in between waves. This is reflected in this study by allowing the albatross to fly at heights close to the flat surface, whereas the UAV is required to keep an arbitrary positive wing tip clearance, which was chosen to be 0.25 m. Third, values of mass and wing area differ, with the UAV being lighter and having less wing area due to its higher aspect ratio wing.

Zhao and Qi's [7] approach of using a point mass flight model with attached forces is adopted in this paper. Figure 2 gives definitions of the forces, speeds, and angles used in the model. The flight model contains translations only and no rotations, as the rotational dynamics are assumed to be significantly faster than the translational

[¶]Selig, M. S., "UIUC Airfoil Coordinates Database–Version 2.0," http://www.ae.uiuc.edu/m-selig/ads/coord_database.html (retrieved 6 May 2008).

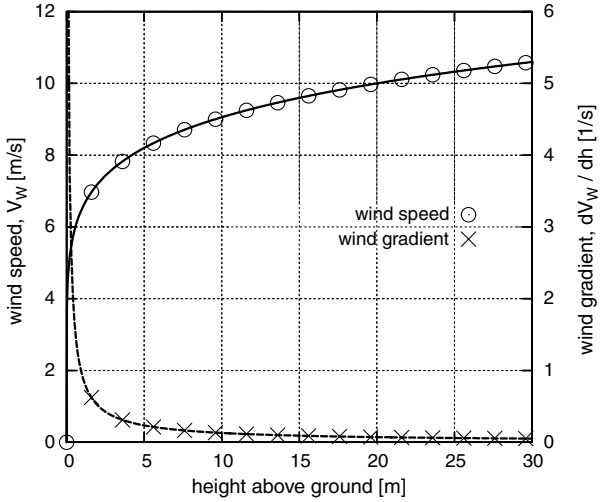

Fig. 1 Wind speed (upper curve) and wind gradient (lower curve).

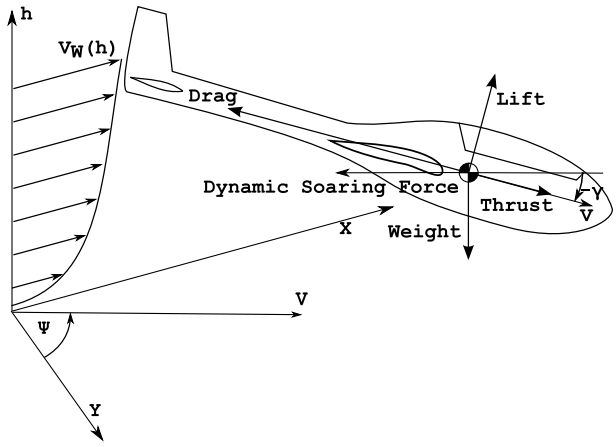

Fig. 2 Flight model angles, speeds, and forces.

dynamics. The flight model thus has 3 DOF. Although engineless flight is considered throughout this paper, engine thrust is included in the model to achieve differential flatness, which is necessary for the optimization approach. Further methods which ensure the trajectories are designed for engineless flight are introduced later.

Table 1 gives numerical values of the flight model's parameters. Values for the albatross have been taken from Sachs [5], while lift and drag values for the SD-7037 aerofoil were computed using Drela's XFOIL [14] and these results were then used to compute lift and drag for the finite wing using nonlinear lifting line theory [15]. The lift-to-drag ratio given in Table 1 is optimistic for a whole vehicle and it would be interesting to revisit the problem with a more accurate vehicle. The UAV's aspect ratio was selected based on good engineering practice and is similar in its value to aspect ratios of radio controlled, large scale gliders. The UAV's mass has been selected after a brief initial investigation with good minimal wind performance in mind. The mass value is comparable to the mass of other small UAVs [16] such as "Avatar P2" by Codarra Advanced Sytems Pty Ltd, "Azimut 2" by Alcore Technologies, and "Carolo P330" by Mavionics GmbH. Unfortunately, the available data did not permit comparing wing loadings.

Table 1 Flight model parameter values

	Albatross [5]	UAV
m	9.5 kg	4.5 kg
b	3 m	3 m
S	0.63 m^2	0.473 m^2
AR	14.3	19.0
C_{D0}	0.033	0.0173
C_{D1}	0.0	−0.0337
C_{D2}	0.019	0.0517
$C_{L,\max}$	1.6	1.1
$(C_L/C_D)_{\max}$	20	33.4
m/S	15.1 kg/m^2	9.5 kg/m^2

The flight model's states are as follows: airspeed $V(t)$, elevation $\gamma(t)$, azimuth $\Psi(t)$, height $h(t)$, (x, y) positions, $r_x(t)$, and $r_y(t)$. The inputs are lift coefficient $C_L(t)$, angle of bank $\mu(t)$, and engine thrust $T(t)$. The model's outputs are identical to the states. Lift $L(t)$ and drag $D(t)$ are expressed as

$$L = \tfrac{1}{2}\rho S C_L V^2 \tag{3}$$

$$D = \tfrac{1}{2}\rho S C_D V^2 \tag{4}$$

where C_D is related to C_L by

$$C_D = C_{D0} + C_{D1} C_L + C_{D2} C_L^2 \tag{5}$$

The UAV's speed, Eqs. (6–8), is modeled in a wind relative reference frame. The UAV's position, Eqs. (9–11), is modeled in an Earth fixed frame. The equations of motion are given by

$$m\dot{V} = T - D - mg\sin(\gamma) - m\dot{V}_W \cos(\gamma)\sin(\Psi) \tag{6}$$

$$mV\cos(\gamma)\dot{\Psi} = \tfrac{1}{2}\rho S C_L V^2 \sin(\mu) - m\dot{V}_W \cos(\Psi) \tag{7}$$

$$mV\dot{\gamma} = \tfrac{1}{2}\rho S C_L V^2 \cos(\mu) - mg\cos(\gamma) + m\dot{V}_W \sin(\gamma)\sin(\Psi) \tag{8}$$

$$\dot{h} = V\sin(\gamma) \tag{9}$$

$$\dot{r}_x = V\cos(\gamma)\sin(\Psi) + V_W(h) \tag{10}$$

$$\dot{r}_y = V\cos(\gamma)\cos(\Psi) \tag{11}$$

Because the wind relative frame is not inertial, a fictitious force [17], F_{DYN}, appears in Eqs. (6–8):

$$F_{\mathrm{DYN}} = -m\dot{V}_W \tag{12}$$

In the following, this force will be referred to as the dynamic soaring force. Although this force is an apparent force, it can be used to do work [17]. A more familiar example of an apparent force is the centrifugal force one can experience on a merry-go-round. Projected onto the UAV's longitudinal axis and combined with Eqs. (2), (9), and (12), gives

$$F_{\mathrm{DYN}} = -m\frac{pV_R}{h}\left(\frac{h}{h_R}\right)^p V\sin(\gamma)\cos(\gamma)\sin(\Psi) \tag{13}$$

Equation (13) shows that to extract energy from the wind gradient the product of $\sin(\gamma)$ and $\sin(\Psi)$ must be negative, i.e., the UAV dives downwind or climbs upwind. If the maneuver is reversed, i.e., upwind dive or downwind climb, the UAV loses energy.

C. Trajectory Optimization Using Differential Flatness

Originally introduced to control theory by Fliess et al. [18] and presented in a textbook by Sira-Ramírez and Agrawal [19], differential flatness is a property of controllable linear and some nonlinear systems, which greatly simplifies trajectory optimization and control. The idea behind differential flatness is to find a closed form of the system's inverse dynamics based on a new set of outputs. One of the major aspects is that the flat outputs are not necessarily identical with the system's usual outputs. The authors found that equations of motion (6–11) are differentially flat only if they are square, i.e., there are as many inputs as outputs. For this reason,

engine thrust is retained in the flight model. Differential flatness simplifies trajectory optimization problems as it maps the input and state space into the space of the differentially flat outputs, which has fewer dimensions [20]. Furthermore, numerical integration of the equations of motion is avoided.

Imagine a nonlinear system of the form:

$$\dot{\mathbf{x}} = \mathbf{f}(\mathbf{x}, \mathbf{u}) \qquad \mathbf{y} = \mathbf{g}(\mathbf{x}, \mathbf{u}) \tag{14}$$

This system is said to be differentially flat if a set of outputs $\mathbf{z}$ exist such that the system's normal outputs $\mathbf{y}$, inputs $\mathbf{u}$, and states $\mathbf{x}$ can be expressed as a function of the flat output $\mathbf{z}$ and its derivatives with respect to time, $\mathrm{d}\mathbf{z}/\mathrm{d}t$, i.e.,

$$\mathbf{x} = \mathbf{h}_1(\mathbf{z}, \dot{\mathbf{z}}, \ddot{\mathbf{z}}, \ldots) \qquad \mathbf{u} = \mathbf{h}_2(\mathbf{z}, \dot{\mathbf{z}}, \ddot{\mathbf{z}}, \ldots)$$
$$\mathbf{y} = \mathbf{h}_3(\mathbf{z}, \dot{\mathbf{z}}, \ddot{\mathbf{z}}, \ldots) \tag{15}$$

The flight model given in Eqs. (6–11) is differentially flat, with $\mathbf{z} = (h, r_x, r_y)$ being the flat output vector. The remaining states (V, Ψ, γ) and control inputs (C_L, μ) can now be expressed as functions of $\mathbf{z}$, $\mathrm{d}\mathbf{z}/\mathrm{d}t$, and $\mathrm{d}^2\mathbf{z}/\mathrm{d}t^2$:

$$V = \sqrt{\dot{h}^2 + (\dot{r}_x - V_W(h))^2 + \dot{r}_y^2} \tag{16}$$

$$\Psi = \arctan\left(\frac{\dot{r}_x - V_W}{\dot{r}_y}\right) \tag{17}$$

$$\gamma = \arcsin\left(\frac{\dot{h}}{V}\right) \tag{18}$$

$$\mu = \arctan\left(\frac{\cos(\gamma)\dot{\Psi} + \dot{V}_W/V\cos(\Psi)}{\dot{\gamma} + g/V\cos(\gamma) - \dot{V}_W/V\sin(\gamma)\sin(\Psi)}\right) \tag{19}$$

$$C_L = \frac{mV\dot{\gamma} + mg\cos(\gamma) - m\dot{V}_W\sin(\gamma)\sin(\Psi)}{(1/2)\rho S V^2\cos(\mu)} \tag{20}$$

$$T = m\dot{V} + D + mg\sin(\gamma) + m\dot{V}_W\cos(\gamma)\sin(\Psi) \tag{21}$$

The selection of suitable basis functions for $\mathbf{z}$ is restricted by the requirement for $\mathbf{z}$ to be twice continuously differentiable with respect to time and because loitering trajectories are periodic, this paper adopts sinusoidal basis functions. To achieve a displacement in the (x/y) plane and thus cross-country flight, the sinusoidal basis functions for $r_x(t)$ and $r_y(t)$ are superimposed with a linear term, giving $h(t)$, $r_x(t)$, and $r_y(t)$ as

$$h(t) = a_{h0} + \sum_{n=1}^{N} a_{hn}\sin\left(\frac{2\cdot\pi\cdot n\cdot t}{t_f} + \eta_{hn}\right) \tag{22}$$

$$r_x(t) = a_{x0} + V_{\mathrm{CC}}\sin(\varepsilon)\cdot t + \sum_{n=1}^{N} a_{xn}\sin\left(\frac{2\cdot\pi\cdot n\cdot t}{t_f} + \eta_{xn}\right) \tag{23}$$

$$r_y(t) = a_{y0} + V_{\mathrm{CC}}\cos(\varepsilon)\cdot t + \sum_{n=1}^{N} a_{yn}\sin\left(\frac{2\cdot\pi\cdot n\cdot t}{t_f} + \eta_{yn}\right) \tag{24}$$

A nonzero V_{CC} term in Eqs. (23) and (24) produces a cross-country trajectory. The linear term is sufficient to model cross-country flight, as the sinusoidal terms in the basis functions allow any perturbation to be added to the linear motions. Such a trajectory (Fig. 5) is still periodic in terms of height and speed and is thus periodic in the UAV's energy. When closed trajectories (Fig. 4) are desired, V_{CC} must be set to zero.

The basis function's parameters together with the wind model's parameters are collected into the design vector $\mathbf{X}$, which then completely describes the trajectory and wind conditions. Any combination of values in $\mathbf{X}$ fulfils the equations of motion but the resulting control and state trajectories may contain undesirable values. Equation (25) shows the design vector for closed trajectories, i.e., V_{CC} is fixed at zero:

$$\mathbf{X} = [a_{h0}, \ldots, a_{hN}, a_{x0}, \ldots, a_{xN}, a_{y0}, \ldots, a_{yN}, \eta_{h1}, \ldots,$$
$$\eta_{hN}, \eta_{x1}, \ldots, \eta_{xN}, \eta_{y1}, \ldots, \eta_{yN}, V_R, t_f]^T \tag{25}$$

The optimization problem can now be stated to be

$$\text{minimize } J(\mathbf{X}) \quad \text{subject to } \mathbf{lb} \le \mathbf{X} \le \mathbf{ub}$$
$$\mathbf{C}_{\mathrm{eq}}(\mathbf{X}) = 0 \qquad \mathbf{C}(\mathbf{X}) \le 0 \tag{26}$$

where $J(\mathbf{X})$ is the value function, $\mathbf{lb}$ and $\mathbf{ub}$ are vectors with box constraints on $\mathbf{X}$, i.e.,

$$\begin{pmatrix} -500 \\ \vdots \\ -500 \\ 0 \\ \vdots \\ 0 \\ 0 \\ 0 \end{pmatrix} \le \begin{pmatrix} a_{h0} \\ \vdots \\ a_{yN} \\ \eta_{h1} \\ \vdots \\ \eta_{yN} \\ V_R \\ t_f \end{pmatrix} \le \begin{pmatrix} 500 \\ \vdots \\ 500 \\ 2\pi \\ \vdots \\ 2\pi \\ 150 \\ 200 \end{pmatrix} \tag{27}$$

$\mathbf{C}_{\mathrm{eq}}$ and $\mathbf{C}$ are nonlinear constraint functions which are used to ensure that the wing tip clearance is strictly positive, the UAV's airspeed is always smaller than $V_{\max}$, and to prevent the UAV's wing from stalling. The trajectory is intended to be engineless, hence the engine thrust $T(t)$ must be constrained in such a way that its value remains in a small band around zero. Equation (28) shows how this is achieved with the aid of the constants $T_{\min}$ and $T_{\max}$:

$$\mathbf{C}(\mathbf{X}, t) = \begin{pmatrix} C_L(t) - C_{L,\max} \\ V(t) - V_{\max} \\ \mu_{\min} - \mu(t) \\ \mu(t) - \mu_{\max} \\ T_{\min} - T(t) \\ T(t) - T_{\max} \\ h_{\min} - h(t) + \frac{1}{2}b\sin(\mu(t)) \\ h_{\min} - h(t) - \frac{1}{2}b\sin(\mu(t)) \end{pmatrix} \le 0 \tag{28}$$

$$\mathbf{C}_{\mathrm{eq}}(\mathbf{X}) = \begin{pmatrix} \Psi(t=0) \\ r_x(t=0) \\ r_y(t=0) \end{pmatrix} = 0 \tag{29}$$

The nonlinear constraints $\mathbf{C}(\mathbf{X}, t)$ are enforced at $M+1$ equally spaced time points and collected into one constraint vector $\mathbf{C}(\mathbf{X})$,

$$\mathbf{C}(\mathbf{X}) = \begin{pmatrix} \mathbf{C}(\mathbf{X}, t=0) \\ \mathbf{C}(\mathbf{X}, t=\frac{kt_f}{M}) \\ \vdots \\ \mathbf{C}(\mathbf{X}, t=t_f) \end{pmatrix} \le 0, \quad k = 1, 2, 3, \ldots, M-1 \tag{30}$$

The distribution of time points must be kept sufficiently fine to prevent the engine thrust curve from forming large peaks between two time points. As the trajectory's rate of change depends on the number of frequency components N, the required number of time points M is related to N and it was found that good results are achieved with $M \ge 5N$ (see Fig. 3).

The value function's form depends on the nature of the dynamic soaring trajectory. To investigate minimal and maximal wind conditions the following value function was used:

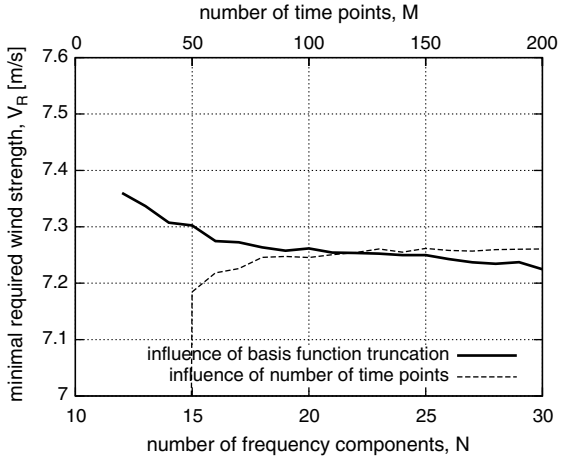

Fig. 3 Influence of the number of frequency components and the number of time points on the optimization result for closed trajectories. The influence of the number of frequency components has been calculated by varying N while setting $M = 5N$. The influence of time point density was calculated by setting $N = 20$ and varying M.

$$J(\mathbf{X}) = \pm V_R \tag{31}$$

where $+V_R$ is used to generate minimal condition trajectories and $-V_R$ for maximal conditions.

If Eqs. (22–24) used an infinite sum, any periodic trajectory could be modeled. The truncation to a finite sum restricts the number of possible trajectories. As a consequence, the optimal trajectory might be impossible to model, if the infinite sum is truncated too early. In practice, the optimization converges for values above $N = 5$, and the quality of the solution does not improve significantly beyond $N = 20$ (see Fig. 3). If not stated otherwise, all results were produced with $N = 20$ and $M = 100$.

The optimization problem has been implemented in AMPL [21] and solved with IPOPT [22], which employs an interior point algorithm. The nonlinear optimization is sensitive to the choice of initial guess $\mathbf{X}_0$ and after some initial experimentation, the best initial guess for stationary trajectories was found to be

$$\mathbf{X}_0 = [1, \quad 0, \quad \cdots \quad 0]^T \tag{32}$$

which results in the figure of eight type trajectory shown in Fig. 4. When the optimizer is initialized with a circular initial guess, a suboptimal circular trajectory is produced. The initial guesses for cross-country trajectories were developed out of stationary trajectories.

D. Model Validation

The authors of this paper reproduced minimum wind strength trajectories for albatrosses previously published by Sachs [5] to validate the flight model and trajectory optimization process. Figure 5 shows a cross-country trajectory for an albatross with parameter values according to Sachs (see Table 1). This trajectory is the absolute minimal requirements trajectory, i.e., the trajectory which results in the lowest required wind strength. Sachs reports a required reference wind speed of 9.4 m/s at 20 m, which compares favorably with 9.5 m/s at 20 m which was computed using our approach. Although the trajectory's general shape is identical, a small difference is found in direction when comparing the two trajectories. Sachs's trajectory has a directional angle of $\varepsilon = 41.3$ deg, whereas our trajectory's direction is $\varepsilon = 36.6$ deg. The difference is likely to be the result of using different optimization software and estimating Sachs's directional angle from trajectory plots. It was also noted that the minimal wind strength strongly depends on the allowed maximum bank angle and minimum height above ground and care has been taken to match values published by Sachs in [5]. Sachs's trajectory has thus been replicated to accuracy of the published material.

III. Closed Trajectories

Closed, or stationary, trajectories represent the operationally important problem of station keeping or loitering. Furthermore, closed trajectories are independent of the wind's direction and are hence of interest for investigating the sensitivity of the minimal and maximal wind conditions to changes in trajectory constraints or to changes of the UAV's physical parameters. A plot of a closed trajectory for minimal wind conditions of the example UAV can be found in Fig. 4.

We investigate the influence of four trajectory constraints on minimal and maximal wind conditions: maximum bank angle, minimum trajectory height, maximum airspeed, maximum lift coefficient, as well as one physical parameter: mass. Since Sachs et al. [4] also identified lift-to-drag ratio as a major factor on dynamic

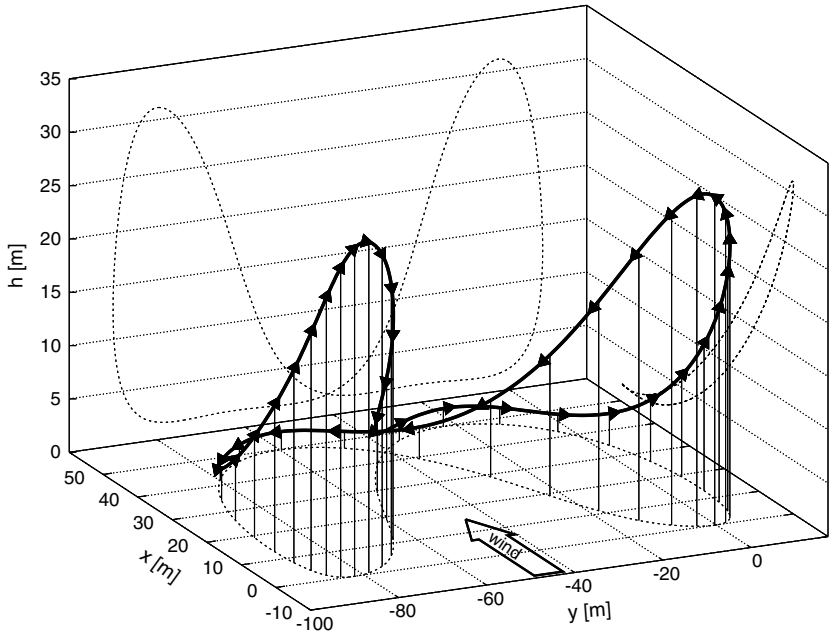

Fig. 4 Minimal wind conditions for closed trajectory example. Wind conditions: $V_R = 7.47$ m/s at $h_R = 20$ m.

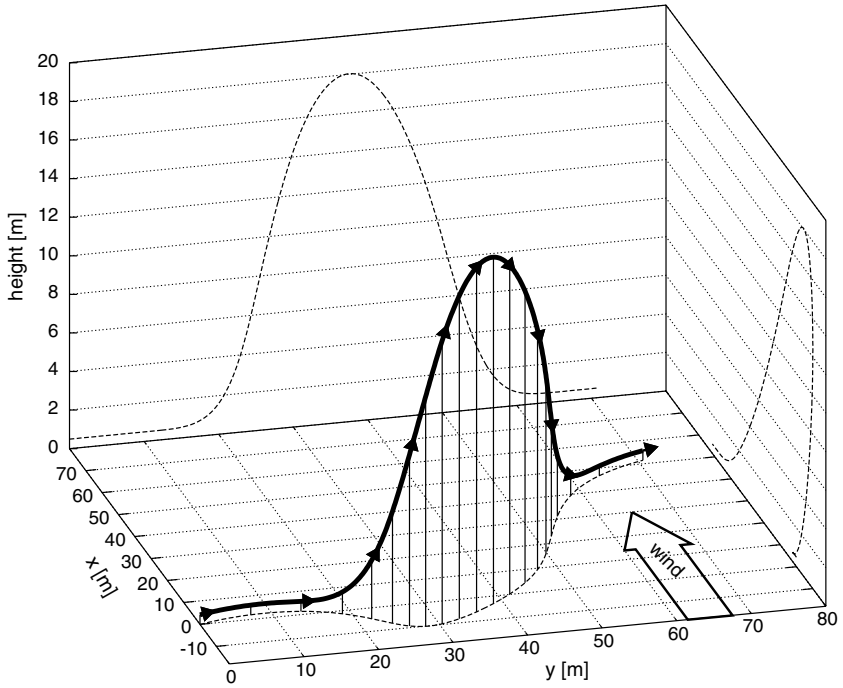

Fig. 5 Absolute minimum wind strength trajectory for an albatross. Wind conditions: $V_R = 9.48$ m/s at 20 m above the surface.

performance, the sensitivity to this parameter is not reexamined here. The sensitivities of the minimal and maximal wind conditions to the trajectory constraints or physical parameters of the flight model have been investigated by repeatedly solving the optimization problem while changing the constraint or parameter under consideration between runs. The result of the last optimization run was reused as the initial guess for the next run.

A. Sensitivity to Lift Coefficient Limit

The lift coefficient's limit $C_{L,\max}$ controls the maximum amount of lift a wing can produce. Sensitivity of the minimal and maximal wind conditions to the lift coefficient limit was investigated by changing the appropriate value in Eq. (28) in between optimization runs. Because $C_{L,\max}$ is a limit only, the optimizer is not required to make use of the full permissible C_L range if doing so results in suboptimal trajectories. It is thus expected that the curves for minimal and maximal wind conditions level off after the optimal value instead of showing clear extrema. Figure 6 shows an improvement of the maximum wind conditions with increased $C_{L,\max}$. The lift coefficient's limit shows a significant effect on the minimum wind conditions at low $C_{L,\max}$ values, which are below the C_L value for which the best glide ratio is achieved (approximately $C_L = 0.578$). Although the maximal wind conditions show a stronger response to $C_{L,\max}$, the effect on the minimal conditions should not be ignored, as it will be shown later on that the minimum conditions contribute strongly to the likelihood of favorable winds.

B. Sensitivity to Angle of Bank Limit

Observations of albatross flight by Pennycuick [14] indicate that dynamic soaring benefits from large bank angles. Flight at high angles of bank can be difficult to control; thus a bank angle limit is desirable from a control point of view. Figure 7 shows the influence of bank angle limit on minimum and maximum wind conditions. Minimum conditions fall with a rising maximum bank angle limit until the curve levels off. Maximum conditions behave similarly but settle at slightly larger angles. A larger maximum bank angle limit increases the turn rate and thus decreases the time required to fly a single orbit. In case of trajectories for minimal wind conditions, increasing the bank angle limit from 37.2 deg to 90 deg reduces the maneuver duration from 20.0 s to 11.1 s. In case of maximal wind condition trajectories, the same change in bank angle limit reduces the maneuver duration from 25.0 s to 20.7 s. As a result less energy is lost to drag and less energy needs to be extracted from the ambient wind gradient. The drag losses cannot be reduced any further once

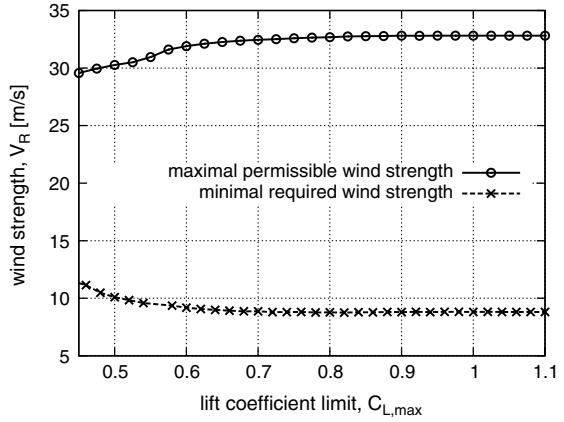

Fig. 6 Influence of the lift coefficient limit, $C_{L,\max}$, on maximal and minimal wind conditions for closed trajectories.

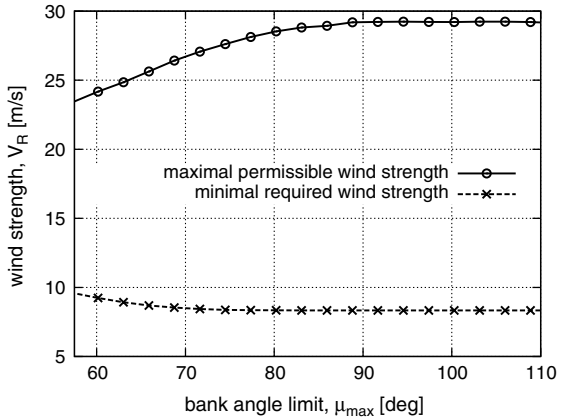

Fig. 7 Influence of bank angle limit, $\mu_{\max}$, on maximal and minimal wind conditions for closed trajectories.

the highest turn rate is achieved. Both curves in Fig. 7 show that bank angles between 75 deg and 90 deg are the most desirable from a performance point of view.

C. Sensitivity to Airspeed Limit

To close its trajectory an aircraft must fly faster than the prevailing winds so that the downwind drift can be compensated for. Figure 8 shows that the UAV can fly in wind conditions up to reference wind speeds V_R of 1 m/s less than its airspeed limit. The UAV's drag losses are a function of the airspeed's square and this raises the question how enough energy can be extracted to sustain flight at high wind speeds. Equation (13) shows that the dynamic soaring force magnitude grows linearly with the UAV's airspeed and the reference wind speed and the combination of increased airspeed limit and increased reference wind speed is able to compensate for the drag losses.

As it is the aim to decrease the reference wind speed in the case of the minimal wind conditions, the increase in drag with increased airspeed cannot be compensated for in the same way and thus the optimization produces trajectories which do not use the full range of permissible airspeeds. Thus the minimal wind condition curve in Fig. 8 levels off after some initial improvement.

D. Sensitivity to Ground Clearance

Figure 1 shows that the wind gradient's magnitude quickly increases with reduced height and Eq. (13) shows the dependence of the dynamic soaring force on the gradient's magnitude. Hence wing tip clearance has a major influence on minimal and maximal wind conditions. Figure 9 shows that both minimal and maximal wind conditions improve with smaller wind tip clearances. Although flying in such close proximity to the surface increases the difficulty of the already nontrivial control problem, observations of albatross flight [14] indicate significant performance benefits.

E. Sensitivity to UAV Mass

The influence of mass on minimal and maximal wind conditions was investigated by repeatedly finding optimal trajectories for minimal and maximal wind conditions while changing the mass value in between optimization runs. Because the UAV's mass is a fixed parameter, it is not subject to the optimization and is therefore excluded from $\mathbf{X}$. A suboptimal value of m cannot be corrected by the optimization process and it is thus expected that the curves for minimal and maximal wind conditions in Fig. 10 do not level off but show minima and maxima. Increasing the UAV's wing loading improves the maximal wind conditions up to the maximal value of V_R, which appears at 7.5 kg, after which V_R reduces with further increases in mass. The curve of the minimum wind conditions in Fig. 10 shows a minimum at about 3.5 kg. Two effects influence these curves: the amount of extractable energy and drag losses. Let us consider the minimal wind conditions first. Figure 11 shows that a higher mass results in higher average C_L values as the wing must produce more lift and as a result higher lift coefficients are used which cause more induced drag [Eq. (5)]. The reduction of minimal wind conditions observed at high wing loadings occurs due to this increase of drag. The dynamic soaring force's magnitude depends linearly on the UAV's mass as well as on the reference wind speed [Eq. (13)]. Low mass values thus require flight in stronger winds to

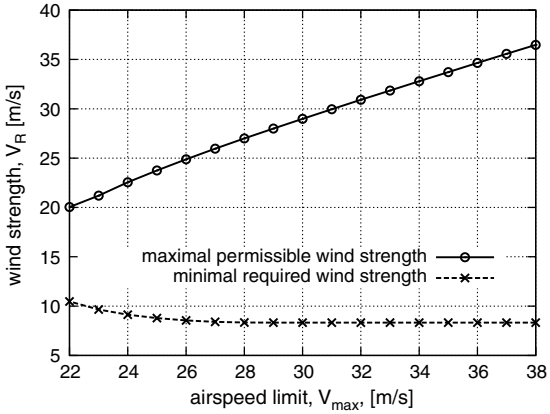

Fig. 8 Influence of air speed limit, $V_{\max}$, on optimization results for closed trajectories.

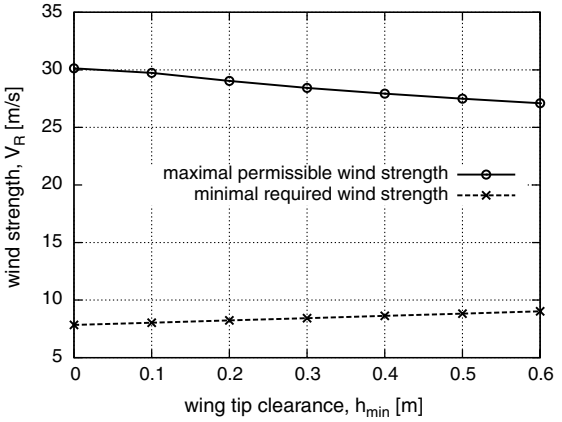

Fig. 9 Influence of wing tip clearance, $h_{\min}$, on maximal and minimal wind conditions for closed trajectories.

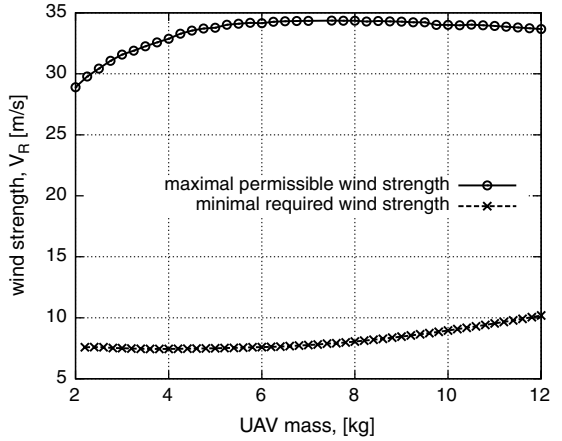

Fig. 10 Influence of UAV mass on maximal and minimal wind conditions for closed trajectories.

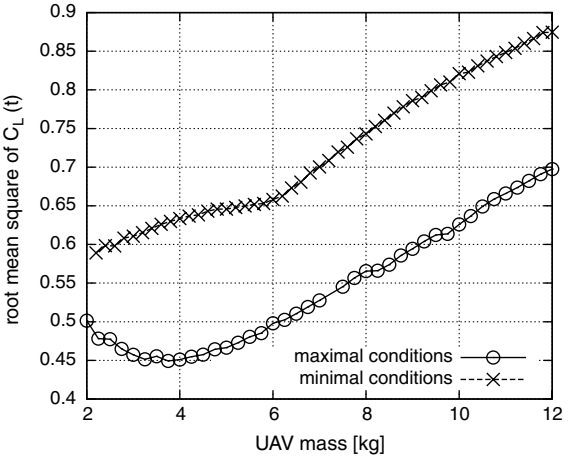

Fig. 11 Geometric mean of $C_L(t)$ plotted against UAV mass for minimal and maximal wind condition trajectories. The kink around 6 kg in the minimal conditions curve occurs because of the airspeed reaching its maximum constraint, $V_{\max}$.

compensate. The combination of these two effects causes the minima in the required wind condition curve. The same two effects occur when maximal wind conditions are considered. Strong winds require fast flying to compensate for drift and to close the trajectory. Drag increases with the airspeed's square which makes fast flight expensive in terms of energy loss. As mentioned before, the extractable energy is limited at low mass values. Thus the UAV cannot fly in the strongest winds when its mass is low. High mass values cause increased drag due to use of high lift coefficients (Fig. 11). As shown in Eqs. (4) and (5), drag depends on the lift coefficient and airspeed and as a result, the combination of high mass and high speed flight leads to high drag losses and thus reduced maximal wind conditions.

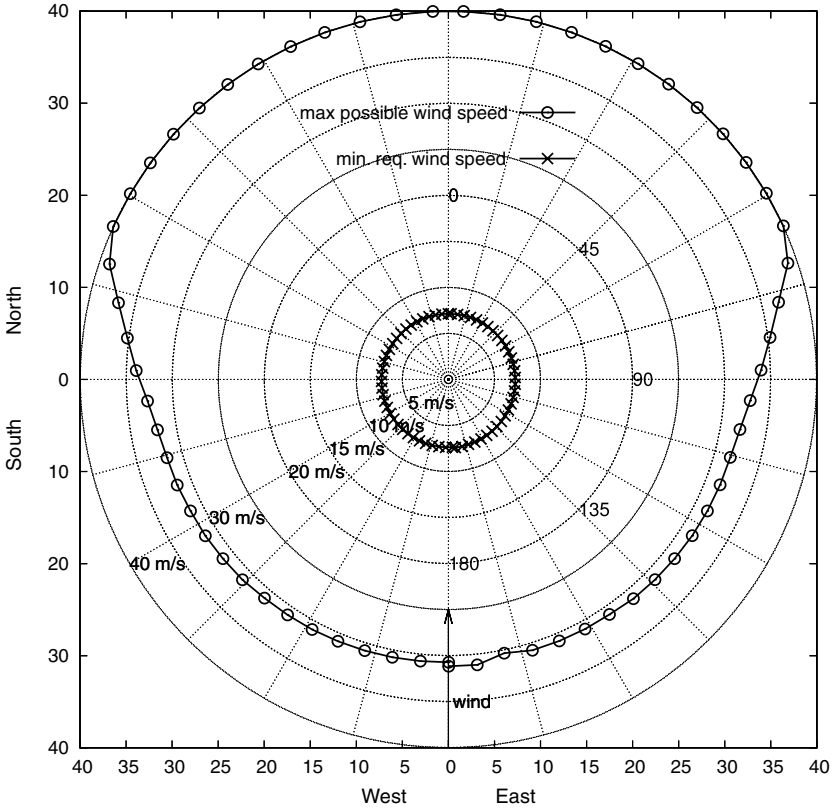

Fig. 12 Minimal and maximal wind conditions (at $h_R = 20$ m) that permit a ground speed of at least 0.5 m/s for the SD 7037 aerofoil UAV.

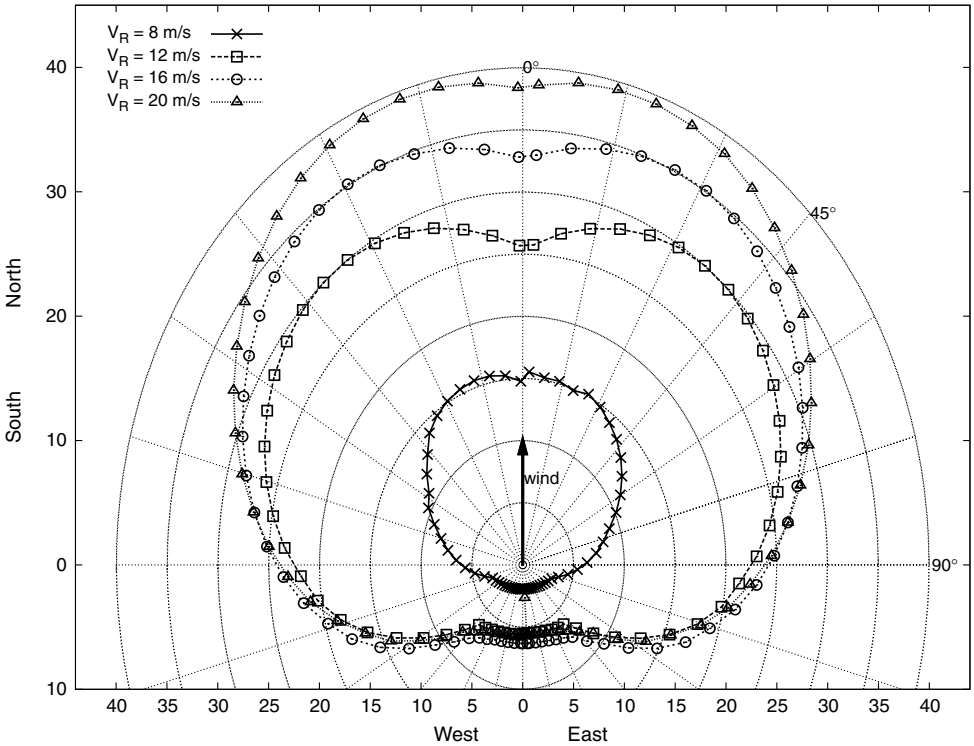

Fig. 13 Optimal cross-country travel rates, V_{CC}, for the UAV at selected wind speeds, V_R, at $h_R = 20$ m. The following parameters were used: $N = 12$ and $M = 50$.

IV. Cross-Country Trajectories

For some UAV applications, engineless flight between two locations is desirable. Such cross-country trajectories are generated by augmenting the sinusoidal basis functions for $r_x(t)$ and $r_y(t)$ with a linear function, i.e., allowing a positive value for V_{CC} in Eqs. (23) and (24). As a result, the trajectory is still periodic in $V(t)$, $\gamma(t)$, $\Psi(t)$, and $h(t)$ but is displaced in the (x, y) plane.

While the desired direction ε is held at a fixed value, the cross-country travel rate V_{CC} is a subject of the optimization and thus part of $\mathbf{X}$. To establish minimal and maximal wind conditions for cross-country flight, the value function of Eq. (31) is used. The minimal and maximal wind conditions depend on the direction of travel relative to the wind ε in Eqs. (23) and (24) (Fig. 12). The minimal wind conditions change from $V_R = 7.43$ m/s for upwind flight to $V_R = 7.13$ m/s for downwind flight and are thus only weakly dependent on direction. The maximal wind conditions behave differently, increasing from $V_R = 31.9$ m/s for upwind travel to $V_R = 34.0$ m/s for travel at right angles to the wind. For directions of less than 60 deg, upper boundary wind speeds become very large and have been artificially limited to 40 m/s to prevent clutter in the diagram. Note that minimal wind strength trajectories result in low cross-country travel rates, especially for upwind travel. To prevent the resulting trajectories from becoming closed trajectories, the cross-country speed was constrained by $V_{CC} \geq 0.5$ m/s.

The maximal permissible wind speeds for cross-country flight in downwind directions are significantly higher than the permissible wind speeds for stationary trajectories. This indicates an option for dealing with higher than expected winds. If the wind exceeds the maximal permissible wind strength for stationary flight, allowing downwind drift permits finding trajectories during high winds. The maximal permissible wind strength for stationary flight may be increased by using engine assisted dynamic soaring as proposed by Zhao and Qi [7], however, this is left to future research.

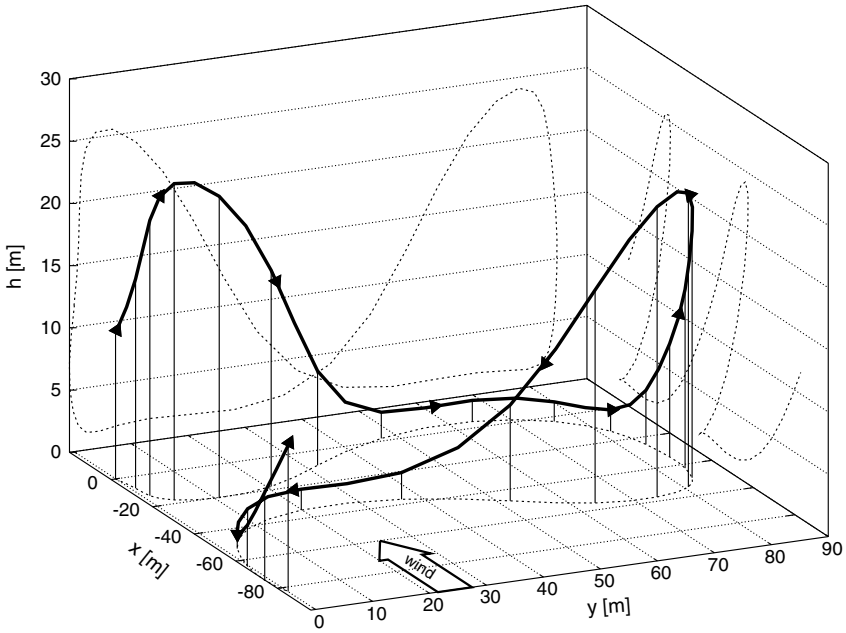

Fig. 14 Optimal upwind trajectory with $V_R = 12$ m/s at $h_R = 20$ m.

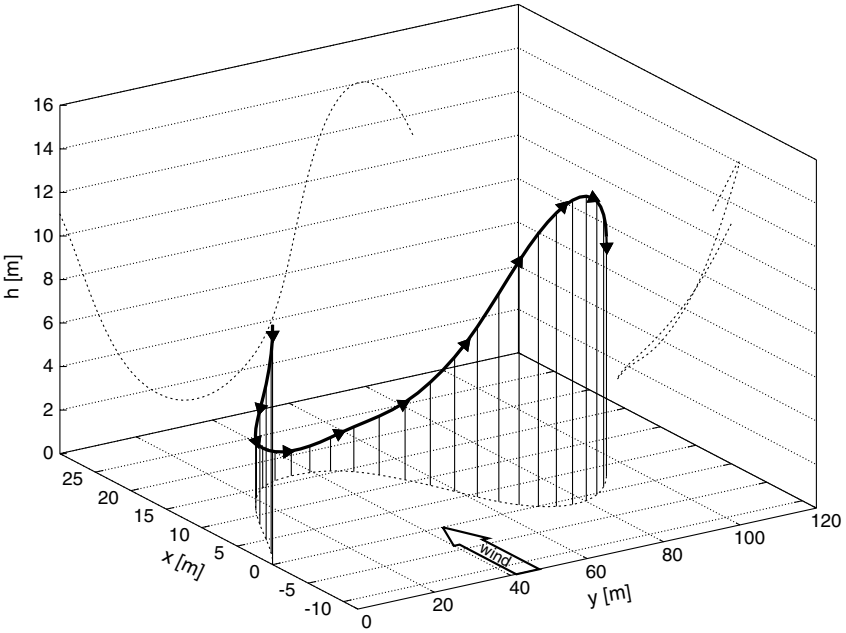

Fig. 15 Optimal cross-wind trajectory with $V_R = 12$ m/s at $h_R = 20$ m.

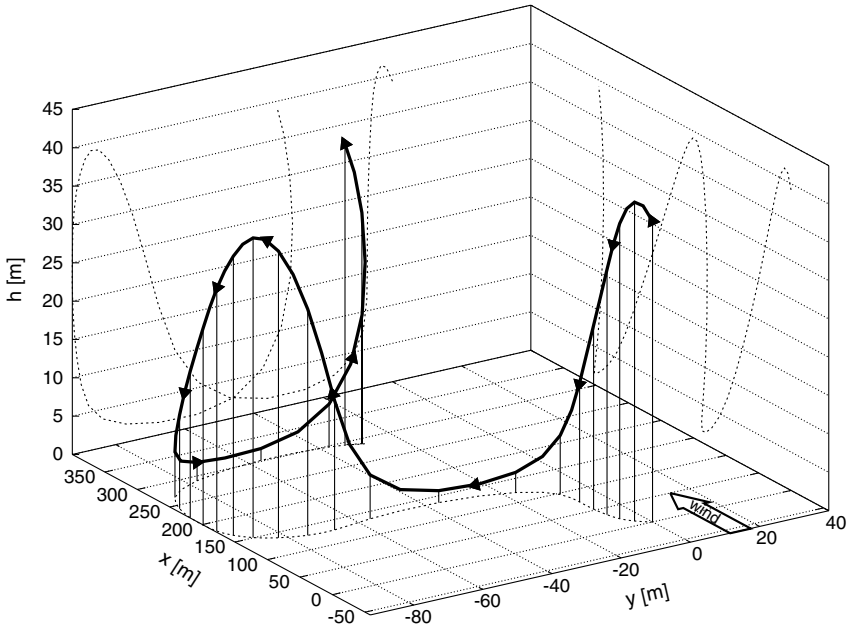

Fig. 16 Optimal downwind trajectory with $V_R = 12$ m/s at $h_R = 20$ m.

Higher cross-country travel rates are expected to be possible when flying at winds from the middle of the favorable wind speed range. Investigation of the achievable cross-country travel rates V_{CC} requires a change to the optimization problem. V_R is now a constant and is thus replaced in the design vector, Eq. (25), by V_{CC}. The value function thus becomes

$$J(\mathbf{X}) = -V_{CC} \tag{34}$$

Figure 13 shows cross-country speeds the UAV can achieve at given directions and wind speeds. Please note that the lines cross in the upwind sector and the best upwind speed is reached at a reference wind speed of $V_R = 16$ m/s. These curves were computed using Eq. (34) as the value function and stepping through the directions ε while prescribing the reference wind speed V_R. The trajectory of the previous direction is then used as the next initial guess. The optimization's result depends on the initial guess, especially so if the initial guess's trajectory curves in a suboptimal direction. This effect appears each time a major axis is crossed. To compensate, the optimization has been repeated for each direction and wind strength with different initial guesses and the best result was used in Fig. 13. As a result, the curves in Fig. 13 are partly nonsmooth.

Figures 14–16 show typical cross-country trajectories for three cases: flight upwind, flight across the wind, and downwind flight. Dynamic soaring enables engineless flight directly upwind and does not need to revert to tacking as sailing yachts do. This is achieved by climbs into the wind and dives across the wind while the connecting turns are largely flown at constant height. Trajectories for flight across the wind show a distinct s shape. In contrast to upwind trajectories, little time is spent at low altitude. Downwind trajectories consist of downwind dives and crosswind climbs. Although a climb across the wind does not extract energy from the wind gradient, the

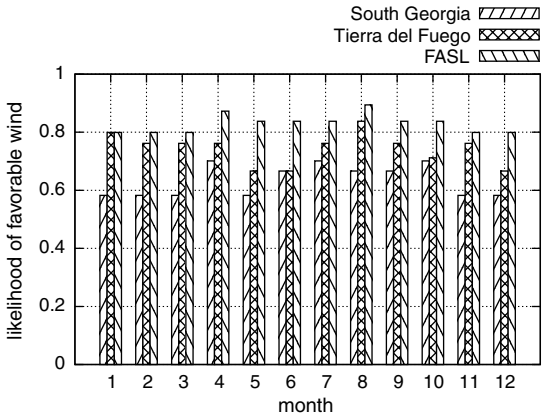

Fig. 18 Probability of favorable winds for a small UAV at three locations in the Antarctic Ocean for each month of the year.

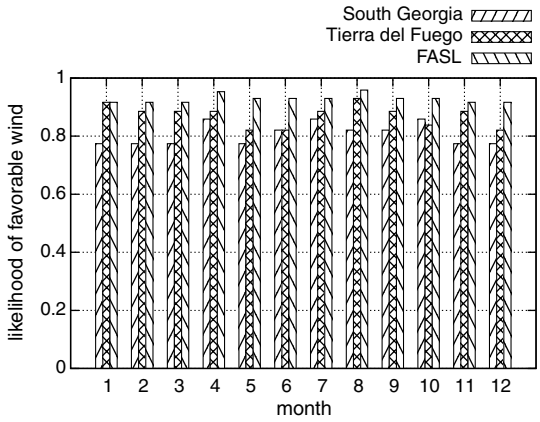

Fig. 17 Probability of favorable winds for an albatross at three locations in the Antarctic Ocean for each month of the year.

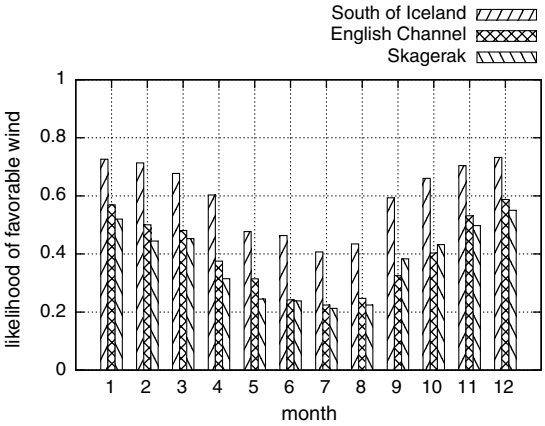

Fig. 19 Probability of favorable winds for a small UAV at three locations in the northern hemisphere for each month of the year.

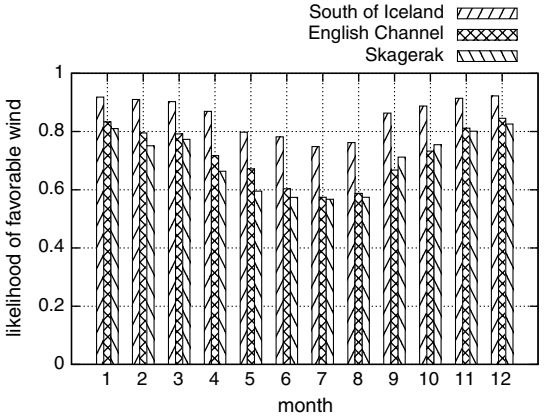

Fig. 20 Probability of favorable winds for a small UAV, which can fly in between waves at three locations in the northern hemisphere for each month of the year.

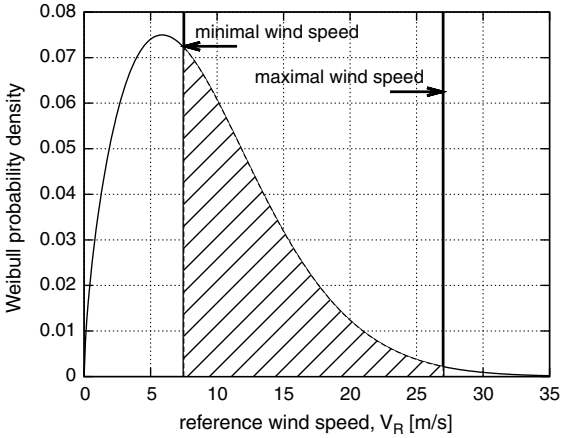

Fig. 21 Probability density function of the wind distribution south of Iceland in September ($\bar{V}_R = 9.2$ m/s, $\sigma = 4.5$ m/s). The shaded area equals likelihood of favorable wind.

large amount of energy extracted by the downwind dive allows for a very high cross-country speed.

V. Likelihood of Favorable Winds

A weather dependent propulsion system must answer the question of how frequently suitable conditions occur. Knowledge of minimal and maximal wind conditions, together with long term weather statistics, allows computation of the likelihood of favorable winds. Weather statistics for all major maritime locations can be found in the KNMI/ERA-40 Wave Atlas** and statistics for the North Sea and Norwegian Sea, in particular, are given by Børresen [23]. These sources assume that the wind speed follows a Weibull distribution and provide mean wind speed and standard deviation for each month of the year.

The wandering albatross in its natural habitat, the Antarctic Ocean, will serve as the baseline case against which the likelihood of favorable weather for the UAV in other locations will be judged. Figure 17 shows likelihoods of favorable winds for the albatross flying stationary trajectories in three locations: the southern tip of South America (Tierra del Fuego), South Georgia, and the French Southern and Antarctic Lands. It can be seen from the graph that the albatross consistently achieves likelihoods between 75 and 90%. Please note that these calculations only consider dynamic soaring and no secondary flight techniques that albatrosses might use. The feasible speed range for dynamic soaring by an albatross has been found by using the parameters for the albatross in Table 1 in the minimum and maximum wind speed optimization of Sec. III. To reflect the albatross' superior flying skill the minimum height limit was set to zero.

Figure 18 shows the likelihood of favorable winds at the same three locations in Antarctica for the UAV. The diagram shows that the UAV, despite its superior aerodynamic efficiency, is clearly inferior compared to the albatross. This indicates that the ability to fly close to the surface is a key factor governing dynamic soaring performance.

The likelihood of favorable winds for the UAV has also been calculated for three candidate locations which the authors believe to be more interesting from an application point of view than the Antarctic Ocean. These are the North Atlantic just south of Iceland, the English Channel, and the Skagerak (north of the peninsula of Jutland). Figure 19 shows the likelihood of favorable winds for the conventional UAV and it is clear from the graph that the likelihood is low, especially for the less windy areas like the English Channel and the Skagerak.

Flying in between waves, as the albatross does, would take a dynamic soaring UAV closer to the region of large wind gradients and improve minimal wind conditions. Hence its likelihood of favorable weather would increase. The effect of flight in between the waves on performance has been estimated by setting $h_{\min}$ to zero. Figure 20 shows improvement of the likelihood of favorable winds to values between 55 and 85%. Clearly this mode of flight would place significant additional demands on the UAV control system, not least the need to accurately determine the wave positions.

The designer of a specialist dynamic soaring UAV is faced with the choice whether to optimize for flight in minimal or maximal wind conditions. Figure 21 shows the probability density function of the wind distribution south of Iceland in September. The striped area under this graph, between the minimal and maximal wind condition lines, equals the likelihood of favorable winds for dynamic. Because of the shape of the distribution, a small reduction of the minimal wind conditions increases the likelihood more than an equal increase in maximal conditions. Thus, when designing a UAV attention should be placed on reducing the minimal wind conditions.

VI. Conclusions

Dynamic soaring gives a small UAV the ability to achieve energy independent loiter and travel behavior, thus prolonging its endurance. For trajectories across the wind and downwind, cross-country speeds are significantly larger than the wind speed. For upwind flight, speeds are smaller than the wind speed but at 5–6 m/s; these are still significant. The full range of feasible wind speeds has been established, from which the likelihood of favorable winds was then computed. Maximizing the likelihood of fair wind requires reducing the minimal wind conditions. With current control technology, the likelihood of favorable winds ranges from 20 to 40% for European waters. Hence, it would be appropriate for dynamic soaring to be used as an auxiliary means of propulsion in an opportunistic fashion.

Physical requirements for dynamic soaring are similar to requirements for powered long endurance flight, namely, low-drag high-aspect ratio wings, low mass, and high lift wings. Analysis of the wind strength probability density function shows that emphasis should be placed on achieving dynamic soaring flight at low wind speeds. Investigation into cross-country flight indicates that dynamic soaring is feasible at strong winds and that high wind periods can be handled by allowing the UAV to drift downwind.

A key enabling feature is the ability to fly very close to the surface in the region of the strongest wind gradient. For maritime applications this might even mean flight "below" the surface by going in between waves. In addition to the performance, which can be achieved with the current level of technology, dynamic soaring UAVs will benefit significantly from further research into advanced flight control and sensors.

Dynamic soaring would profit from further research work investigating the airflow over water surfaces, including the flow in between waves. For practical applications an important source of

**KNMI/ERA-40 WAVE ATLAS, Koninklijk Nederlands Meteorologisch Instituut, http://www.knmi.nl/onderzk/oceano/waves/era40/license.cgi (retrieved 20 May 2008).

uncertainty is not only the wind gradient's magnitude but also its shape and the shape's influence on performance is of interest. Furthermore, an investigation with a flight model with 6 DOF would be useful to investigate the influence of rolling and pitching dynamics on dynamic soaring flight. This higher fidelity would also allow us to investigate and potentially optimize the design of the UAV for particular conditions.

Acknowledgments

The authors express grateful thanks to Alison Eele for her help and support in implementing the optimization problem in AMPL. This research project is financially supported by the Leverhulme Trust under Grant No. F/00 577/F.

References

[1] "Unmanned Aircraft Systems Road Map 2005–2030," United States Department of Defense, July 2005, p. 51.

[2] Croxall, J. P., Silk, J. R. P., Philips, R. A., Afanasyev, V., and Briggs, D. P., "Global Circumnavigations: Tracking Year-Round Ranges of Nonbreeding Albatrosses," *Science*, Vol. 307, Jan. 2005, p. 249. doi:10.1126/science.1106042

[3] Lord Rayleigh, "The Soaring of Birds," *Nature (London)*, Vol. 27, 1883, pp. 534–535.

[4] Sachs, G., Lesch, K., and Knoll, A., "Optimal Control for Maximum Energy Extraction from Wind Shear," *AIAA Guidance, Navigation and Control Conference*, AIAA, Washington, D.C., 1989, pp. 556–564.

[5] Sachs, G., "Minimaler Windbedarf fuer den Segelflug der Albatrosse," *Journal für Ornithologie*, Vol. 134, No. 4, 1993, pp. 435–445. doi:10.1007/BF01639834

[6] Zhao, Y., "Optimal Patterns of UAV Dynamic Soaring," *Optimal Control Applications and Methods*, Vol. 25, No. 2, 2004, pp. 67–89. doi:10.1002/oca.739

[7] Zhao, Y., and Qi, Y. C., "Minimum Fuel Powered Dynamic Soaring of Unmanned Aerial Vehicles Utilizing Wind Gradients," *Optimal Control Applications and Methods*, Vol. 25, No. 5, 2004, pp. 211–233. doi:10.1002/oca.744

[8] Gill, P. E., Murray, W., Sunders, M. A., and Wright, M. H., "User's Guide for NPSOL (Ver. 4.0): A Fortran Package for Nonlinear Programming," Stanford University TR SOL 86-2, 1986.

[9] Utgoff, V., and Johnson, F., "Dynamic Soaring in the Atmospheric Boundary Layer," *XV Organisation Scientifique et Technique du Vol à Voile Congress*, OSTIV, Delft, The Netherlands, 1976.

[10] Gordon, R. J., "Optimal Dynamic Soaring for Full Sized Sailplanes," M.S. Thesis, United States Air Force Institute of Technology, 2006.

[11] Panofsky, H. A., and Dutton, J. A., *Atmospheric Turbulence Models and Methods for Engineering Applications*, Wiley, New York, 1984, p. 131.

[12] Hsu, S. A., Meindl, E. A., and Gilhousen, D. B., "Determining the Power-Law Wind Profile Exponent Under Near-Neutral Stability Conditions at Sea," *Journal of Applied Meteorology*, Vol. 33, June 1994, pp. 757–765. doi:10.1175/1520-0450(1994)033<0757:DTPLWP>2.0.CO;2

[13] Pennycuick, C. J., "Gust Soaring as a Basis for the Flight of Petrels and Albatrosses," *Avian Science*, Vol. 2, No. 1, 2002, pp. 1–12.

[14] Drela, M., "XFOIL: An Analysis and Design System for Low Reynolds Number Airfoils," *Conference on Low Reynolds Number Airfoil Aerodynamics*, University of Notre Dame, South Bend, IN, June 1989.

[15] Sivells, J. C., and Neely, R. H., "Method for Calculating Wing Characteristics by Lifting-Line Theory Using Nonlinear Section Lift Data," NACA TN 1269, April 1949.

[16] Lake, D. (ed.), *Unmanned Vehicles Handbook 2009*, The Shephard Press, Slough, U.K., 2009, pp. 9–22.

[17] José, J. V., and Saletan, E. J., *Classical Dynamics: A Contemporary Approach*, Cambridge University Press, Cambridge, England, 1998, pp. 39–40.

[18] Fliess, M., Lévine, J., Martin, P., and Rouchon, P., "Flatness and Defect of Nonlinear Systems: Introductory Theory and Examples," *International Journal of Control*, Vol. 61, No. 6, 1995, pp. 1327–1361. doi:10.1080/00207179508921959

[19] Sira-Ramírez, H., and Agrawal, S. K., *Differentially Flat Systems*, Marcel Dekker Ltd., New York, 2004.

[20] Petit, N., Milam, M. B., and Murray, M. B., "Inversion Based Constrained Trajectory Optimisation," *5th International Federation of Automatic Control Symposium on Nonlinear Control Systems*, IFAC, Oxford, England, U.K., 2001.

[21] Fourer, R., Gay, D. M., and Kernighan, B. W., *AMPL: A Modeling Language for Mathematical Programming*, 2nd ed., Thomson/Brook/Cole, Florence, KY, Nov. 2002.

[22] Wächter, A., and Biegler, L. T., "On the Implementation of a Primal-Dual Interior Point Filter Line Search Algorithm for Large-Scale Nonlinear Programming," *Mathematical Programming*, Vol. 106, No. 1, 2006, pp. 25–57. doi:10.1007/s10107-004-0559-y

[23] Børresen, J. A., *Wind Atlas for the North Sea and the Norwegian Sea*, Norwegian University Press, Oslo, May 1987, pp. 113–124.